An Improved Microwave Radiative Transfer Model for Tropical Oceanic Precipitation

JEFFREY R. TESMER

Fleet Numerical Meteorology and Oceanography Center, Monterey, California

THOMAS T. WILHEIT

Department of Meteorology, Texas A&M University, College Station, Texas

(Manuscript received 5 December 1995, in final form 16 April 1997)

ABSTRACT

In preparation for the launch of TRMM, new algorithms must be created that take advantage of the combined data from radar and microwave radiometers that will be on board the satellite. A microwave radiative transfer algorithm with a one-dimensional cloud model is created that incorporates data from radar and radiometers using data obtained from TCM-90 and TOGA COARE flown over the western Pacific in 1990 and 1993, respectively.

A hybrid cloud model (HCM) was developed using observations from TOGA COARE, TCM-90, and other field projects. The HCM is a physically based model that is not ''tuned'' by limited ''ground truth.'' Therefore, the HCM incorporated new microphysical data based on observations of clouds. Cloud observations changed the HCM in four ways. First, stratiform clouds with low rain rates were shown to have a low cloud liquid water content (<0.1 g m^{-3}). Second, radar data showed a linear decrease in the logarithm of the backscatter of ice particles above the freezing level. Third, tropical clouds contained more small drops and fewer large drops than predicted by the Marshall–Palmer drop size distribution. Last, the angular distribution of reflected radiation from ocean surface appears to be specular.

The HCM is compared to the Wilheit et al. model (WILM). The HCM differs from the WILM at low rain rates by as much as 10 K. At high rain rates, the HCM and the WILM produce similar brightness temperatures. However, this result is fortuitous because both models have substantially different thermodynamics and microphysics incorporated into them. Next, the brightness temperatures generated by the HCM are compared to observations from TOGA COARE. It is found that the brightness temperatures produced by the HCM closely agree with the observations. This study shows that a plane-parallel microwave radiative transfer algorithm coupled with a cloud model based on microphysical observations can accurately simulate rainfall observed in the Tropics.

1. Introduction

The ocean dominates the hydrological cycle, occupying nearly three-quarters of the earth's surface. Over the remaining one-quarter of the earth's surface, observational networks and research programs have been concentrated on the continents to study meteorological processes such as rainfall. Tropical oceanic phenomena such as El Niño have shown the importance of the Tropics in dictating rainfall over continents and oceans. Measurements of rainfall in the Tropics are particularly scarce since there is only a small ratio of land to water. Satellites offer a reasonable measurement approach with suitable temporal and spatial coverage to monitor oceanic rainfall.

The Tropical Rainfall Measuring Mission (TRMM) satellite, which will be launched in 1997, will provide improved observations of rainfall over the oceans relative to previous satellites. The TRMM objectives are directed toward our understanding of the hydrological cycle over the tropical oceans. TRMM will have a low altitude of 350 km for better instrumental resolution and a low inclination of 35 deg (the maximum latitude of the satellite's orbit) for increased temporal coverage. The TRMM satellite will use a radar at 14 GHz in conjunction with microwave radiometers at 10, 19, 21, 37, and 85.5 GHz (Simpson et al. 1988). A brief summary of the relevant sensors onboard TRMM is listed in Table 1. The unique overlapping coverage of the radar and radiometers will allow a deeper understanding of rainfall over the oceans. It is seen from Table 1 that the radar's swath width is only one-third of the microwave sensor swath. TRMM algorithm development must take advantage of the information gained from the radar data such as the height of the freezing level and apply it over the remaining two-thirds of the TRMM swath.

In preparation for the data received from the TRMM satellite, two airborne experiments were flown over the western Pacific in 1990 and 1993. The Tropical Cyclone Motion–90 (TCM–90) experiment and the Tropical

Corresponding author address: Jeffrey R. Tesmer, FNMOC, Code 73, 7 Grace Hopper Road, Stop 1, Monterey, CA 93943.
E-mail: Tesmerj@fnoc.navy.mil

TABLE 1. Description of the radiometer and radar that will be onboard TRMM (from Simpson et al. 1988).

TRMM Microwave Imager (TMI)	Radar
10.65 GHz V,H	13.8 GHz
19.35 GHz V,H	
21.3 GHz V	4-km footprint
37 GHz V,H	250-m range resolution
85.5 GHz V,H	220-km swath width
760-km swath width	

Ocean Global Atmosphere Coupled Ocean–Atmosphere Response Experiment (TOGA COARE) created an opportunity to integrate airborne radar data with collocated microwave radiometers as the aircraft flew over highly organized systems such as typhoons and through less organized smaller-scale tropical cloud systems. The experiments contained radars and microwave sensors at frequencies and viewing geometries very similar to the TRMM instruments. Rainfall algorithm development using the collocated radar and radiometer data should give a better estimate of rainfall than just radiometer data alone.

Microwave rainfall algorithms rely heavily on the details of the radiative transfer models used to produce them. The recent trend in modeling has been to use the output of multidimensional cloud models as input for the radiative transfer algorithms. The radiative transfer models such as the model discussed in Wilheit et al. (1977) only used a single atmospheric profile for a range of rain rates. The idea that one-dimensional cloud models were apparently too simple to model the real atmosphere led to the appearance of more sophisticated multidimensional cloud models.

Two- and three-dimensional cloud models have been developed to simulate realistic microphysics and precipitation-sized particles for use in convective-scale radiative transfer modeling. Mugnai and Smith (1988) and Smith and Mugnai (1988) used a sophisticated two-dimensional cloud model that evolved over time to study frequencies ranging from 19 to 231 GHz within their plane-parallel radiative transfer model. The cloud model produced large amounts of cloud liquid water (CLW), that was found to mask the rain layer below the freezing level. The large amount of CLW in tall nonprecipitating clouds produced erroneous rainfall amounts in the retrieval. They also found that the evolution of the cloud played an important part in their results. Changes in the CLW and drop size distribution (DSD) over the lifetime of the cloud produced large differences in the brightness temperature–rain rate (T–R) relationships.

Adler et al. (1991) used a three-dimensional cloud model to study the effect of cloud evolution on microwave T–R relationships at 10, 19, 37, and 86 GHz. The case study involved a mesoscale convective system (MCS) that evolved over time to produce areas of convective and stratiform precipitation. The 1.5-km horizontal resolution allowed the authors to examine the role the changing CLW and ice distributions had on the T–R relationship. Their results showed that a three-dimensional model was needed to resolve the CLW and ice distributions within the convective and stratiform regions in the system. They found that CLW and ice played a significant role in the T–R relationships. The fluctuations of ice in the system caused large deviations in the upwelling brightness temperatures at the higher frequency channels. The ice effect was further complicated by CLW masking the scattering signature when it was distributed near the tops of the clouds. Since the amount and distributions of ice changes for both convective and stratiform structure, the life cycle of the system played an important part in the results.

Smith et al. (1992) and Mugnai et al. (1993) used a hybrid statistical–physical precipitation algorithm containing a three-dimensional cloud model. The authors concluded that a high-resolution three-dimensional cloud model was necessary in order to understand the microphysics of clouds. Use of the three-dimensional cloud model showed that frequencies >19 GHz could not sense the low-level rainfall due to the emission and attenuation process above the freezing level. The T–R relationships were affected by the CLW, ice particles, and supercooled water in the upper levels of the cloud. They also found that the vertical distribution of particles within the cloud had a large impact on upwelling brightness temperatures.

One of the biggest problems with multidimensional cloud models is that they are too computationally intensive. Recent papers by Bauer and Schluessel (1993) and Kummerow and Giglio (1994a, b) have tried to speed up the process by selecting a finite number of cloud models based on stratiform or convective structure. The algorithms select a particular cloud model that fits the geophysical situation. Bauer and Schluessel pointed out that their use of multiple cloud models oversimplified the atmosphere. However, their results showed that the vertical liquid water profile and vertical rain rate distribution could be simplified without significant error.

The algorithm used by Kummerow and Giglio selected various types of stratiform and convective cloud structures based on the climatic freezing level. The determination of which cloud structure to use was left up to the algorithm. This technique worked well when high-resolution data from aircraft was used. However, as resolution degraded, the algorithm had trouble with rainfall patterns below the resolution of the radiometer footprint. The authors concluded that this problem was contained in either the cloud structure selection process itself or was due to the three-dimensionality of the radiative transfer problem.

The cloud model developed in this paper represents a middle ground between the Wilheit et al. (1977) model and the multidimensional cloud models used in Adler et al. (1991) and Mugnai and Smith (1988). One-di-

mensional cloud models such as the one used by Wilheit et al. are too simple in handling the microphysical and vertical structure of the cloud. The radiative transfer models that use multidimensional cloud models are very complicated and probably too sophisticated to allow any meaningful interpretation of important variables involved in microwave radiative transfer. The cloud model developed in this paper is one-dimensional, integrated along the vertical axis. A one-dimensional cloud model allows the variables to be fully understood so that knowledge is gained about what is happening to the upwelling brightness temperatures. The model presented in this paper represents an intermediate step between the very complex models discussed above and the excessively simple model of Wilheit et al. By attempting to use this model in rainfall algorithms and by directly testing its assumptions experimentally, one hopes to develop insight as to which complications are important.

The main objective of this paper is to develop a better microwave radiative transfer algorithm using radar and radiometer data taken from the TCM–90 and TOGA COARE experiments. The improved model is physically based and is not ''tuned'' by surface observations or from radar *Z–R* relationships. Improved microphysical observations of tropical oceanic clouds and reflectivity of the ocean surface are at the core of the improved model. The development of an improved radiative transfer model will involve two steps. First, a radiative transfer model will be created that incorporates well-understood physical principles of the atmosphere. Second, this paper will explore what microphysical changes in the model are forced by the observations. With microphysical changes added to the cloud model, the improved radiative transfer algorithm should be able to reproduce brightness temperatures observed by TOGA COARE microwave sensors.

2. Data

The TCM-90 and the TOGA COARE data used in this study were obtained from the western Pacific in 1990 and 1993, respectively. The TCM-90 experiment contained collocated radar and radiometers on board the NASA DC-8 aircraft. The radar operated at 10 and 34.4 GHz, but only the lower frequency was used in this study. The 10-GHz radar was fixed at nadir with a beamwidth of 5.2°. The sensitivity of the radar was <3 dB*Z*.

The TOGA COARE data used in this study were collected from two sensors onboard the NASA DC-8 aircraft during January–February 1993. Radar data were collected from the Airborne Rain Mapping Radar (ARMAR). The ARMAR measured brightness temperatures and backscatter at a frequency of 13.8 GHz. The antenna had an aperture diameter of 0.4 m with a 3-dB beamwidth of 3.8°. ARMAR also used a small fraction of the time between pulses to function as a 13.8-GHz radiometer. The radiometer had a noise equivalent ΔT (NEΔT) of 1 K. The instrument scanned $\pm 20°$ crosstrack from nadir, producing a 9-km swath at a 12-km altitude. The minimum detectable backscatter at 10 km was 10 dB*Z* (approximately 0.2 mm h^{-1}). Only the nadir brightness temperatures and backscatter from ARMAR were studied here. The second sensor utilized was the Airborne Multichannel Microwave Radiometer (AMMR). AMMR operated at 18.7, 21, and 37 GHz for this experiment. The antenna had a 3-dB beamwidth of 6° at each frequency. The accuracy for the portion of the dynamic range relevant to rain measurements was ± 3 K. The instrumental position was fixed at nadir.

The dataset consisted of 13 missions flown within a two-month period during TOGA COARE. AMMR data were sampled every second, while the ARMAR data at nadir were sampled approximately every 2 seconds. The difference in sampling was due to the ARMAR scanning capability that only allowed a nadir observation every other second as the instrument scanned $\pm 20°$ crosstrack. The ARMAR data were linearly interpolated to match the AMMR dataset. The two datasets were combined with housekeeping data from the Data Acquisition and Distribution System to eliminate data with aircraft pitch or roll $> \pm 5°$ and over land surfaces. Backscatter from ARMAR was calculated at nadir at heights above 1 km over the ocean surface to eliminate range sidelobe contamination near the surface. The retrieved backscatter was then used to calculate a radar-estimated rain rate from a *Z–R* relationship.

3. A hybrid cloud model

The Wilheit et al. (1977) model does not have a realistic atmosphere. If realistic microphysics and thermodynamics were added to a radiative transfer model, would the fundamental concepts behind the Wilheit et al. (1977) model still hold? Will the *T–R* relationships still be valid? To answer these questions, a new plane-parallel radiative transfer model was developed with more realistic convection. The new model retains the physics of the Wilheit et al. model but improves on the thermodynamics and microphysics of the model atmosphere and cloud. The new model and the Wilheit et al. model will be referred to hereafter as the hybrid cloud model (HCM) and WILM, respectively. The HCM integrates the vertical velocity of a parcel along the vertical axis every 100 m. Based on observations of clouds over the western Pacific, the cloud base is set at 0.6 km. The parcel follows a pseudoadiabatic lapse rate until its vertical velocity reaches zero. The parcel's ascent is hindered by entrainment and liquid water loading. The HCM is run using the sounding listed in Table 2. The sounding is representative of average atmospheric conditions over the intensive flux array during TOGA COARE. The environmental freezing level is located at 5 km and the integrated water vapor content (IWVC) is 5.1 g cm^{-2}. The new model assumes a sea surface temperature of 301 K and a water salinity of 35 parts per thousand. Wind speed is set to zero for this paper.

TABLE 2. The TOGA COARE sounding used to initialize the HCM.

Pressure (mb)	Height (km)	Temperature (K)	RH (%)
1007	0.0	301.0	79
1000	0.1	300.9	79
950	0.5	297.0	82
900	1.0	294.2	76
850	1.5	291.6	72
700	3.1	283.0	63
500	5.9	268.4	54
300	9.7	243.2	40
100	16.6	191.1	8

TABLE 3. Cloud top, CLW, and supercooled water thickness (SCWT) for selected rain rates in the HCM.

Rain rate (mm h^{-1})	Cloud top (km)	CLW (g m^{-3})	SCWT (km)
0.25	11.4	0.1	0
1	12.6	0.1	0
3	13.1	0.1	0
5	13.5	0.2	0
7.5	13.7	0.3	0.1
10	14.1	0.5	0.2
15	14.4	0.7	0.3
20	14.6	0.8	0.4
25	14.7	0.9	0.5
50	14.8	1.0	0.6
100	14.9	1.1	0.8
150	15.0	1.2	1.0

The model uses Chang and Wilheit (1979) surface emissivity. The HCM assumes a constant cloud radius with height. As the cloud radius increases the entrainment in the model cloud decreases. Therefore, larger clouds rise higher into the atmosphere since they have lower saturated lapse rates than smaller clouds. As the cloud forms, it modifies the atmosphere by changing the temperature and moisture profiles. The model cloud also shifts the freezing level due to the release of latent heat but the change in the freezing level is <300 m.

The amount and vertical distribution of CLW are handled separately from the thermodynamics. The CLW amount can vary as the rain rate changes and the vertical distribution of CLW can assume any profile. The amount and vertical distribution of CLW influence the upwelling brightness temperatures the most at low rain rates. The precipitation-sized particles within the cloud are dependent on the rain rate. Particles fall at their calculated fall speeds, independent of the updraft velocity. There are three classes of hydrometeors: raindrops, supercooled water, and ice. There is no mixed layer containing both liquid and ice particles. Even though mixed layers exist in nature, the thickness of these layers as well as their location above the freezing level is unimportant for frequencies <37 GHz. All precipitation-sized particles are considered to be spherical. Supercooled water is more important to the upwelling brightness temperatures than ice because liquid water contributes to the rain total rainwater thickness. Since upwelling brightness temperatures are only weakly affected by ice, the ice shape becomes irrelevant so that assuming spherical ice particles causes little error. In nature, there are an infinite variety of ice shapes that are completely unknown; therefore, ice modeling will always remain an approximation. There are other reasons why the ice layer is less important in tropical oceanic clouds, but this will be discussed in more detail later. The total rainwater thickness is defined as the vertical distance in the atmosphere that contains liquid water drops. The rain profile in the HCM is constructed so that it conserves mass (i.e., adjusted for density) between the surface and freezing level. The HCM assumes a constant rain rate from the surface to the freezing level. Therefore, the model does not need to rely on a radar Z–R relationship. Radar reflectivity was only used to adjust the microphysical structure above the freezing level where there is low attenuation.

The HCM assumes that low rain rates (<10 mm h^{-1}) come from stratiform clouds. This is a reasonable assumption since the majority of low rain rate observations comes from stratiform clouds. Therefore, the dynamic range at each frequency can be thought of as a cloud evolution. This concept alters the definition of the microphysics at each rain rate in the HCM. At low rain rates, the microphysics will reflect conditions observed in stratiform clouds, whereas at high rain rates the model will have microphysics characteristic of convective clouds. In contrast, the WILM assumed that all rain rates were a result of convection. The transition between convective and stratiform precipitation is usually defined around 10 mm h^{-1}. However, observations from TOGA COARE have made this distinction less clear. In the HCM, the CLW changes rapidly around a rain rate of 10 mm h^{-1}. The DSD and vertical precipitation structure are not affected by the transition to convective rainfall at 10 mm h^{-1}. The HCM applies a different TOGA COARE cloud structure to each rain rate. This assumption can result in potential errors produced by significant departures in the CLW content, vertical precipitation structure above the freezing level (e.g., warm rain), or DSD. Table 3 shows the cloud top, CLW, and supercooled water thickness (SCWT) for selected rain rates in the HCM using the sounding shown in Table 2. Beamfilling and wind speed are also potential sources of error in the model. The HCM assumes beamfilling and uses plane-parallel radiative transfer. More extensive work is done on the beamfilling problem by Wang (1997). Wind speed error may have an impact on the minimum detectable rain rate but, until more important variables are understood, this is not considered an issue in this study.

4. Changes to the HCM forced by the observations

Three important aspects of clouds will be dealt with because of their importance to upwelling microwave brightness temperatures. First, CLW will be examined

since its amount and vertical distribution within a cloud is important, especially at 37 GHz. Second the vertical precipitation structure will be examined since it affects all the frequencies used in this study at high rain rates. Third, the DSD will be examined since it determines the amount of absorption and scattering produced by precipitation-sized particles in the model atmosphere. The vertical precipitation structure and DSD are related and have an effect on all of the microwave frequencies examined in this study. The *Z–R* relationship is derived from the DSD and is a fundamental way of monitoring the vertical reflectivity structure of the cloud. Finally, the angular distribution of reflected radiation from the ocean surface will be examined using radar data. The angular distribution from the ocean surface has a moderate affect on upwelling brightness temperatures at low rain rates.

a. Changes to the amount and vertical distribution of CLW

Studies of CLW over the oceans have been confined to aircraft observations. Numerous studies have shown that oceanic cells have weaker updraft velocities than continental clouds (Zipser and LeMone 1980; Szoke et al. 1986; Lucas et al. 1994; Jorgensen and LeMone 1989). Zipser and LeMone (1980) studied convective cells during the Global Atmospheric Research Program (GARP) Atlantic Tropical Experiment (GATE). The weak updraft velocities in the cells led them to conclude that little liquid water could exist above 5 km ($-5°$ to $-10°$C) since most of the water would fall out as precipitation or be converted to ice. Szoke et al. (1986) confirmed these observations from a later study using GATE data. Black and Hallett (1986) studied CLW in hurricanes. They also found little CLW above the freezing level. They concluded that the abundance of small ice particles above the freezing level were the result of CLW being converted into ice. Jorgensen and LeMone (1989) used data obtained in the Taiwan Area Mesoscale Experiment (TAMEX). They found that CLW decreased rapidly above the freezing level due to the conversion of liquid water into ice and graupel. Gamache (1990) studied convection near Australia during the Summer Monsoon Experiment (SMONEX). He showed that CLW did not exist at temperatures below $-10°$ to $-22°$C. The CLW content never exceeded 0.2 g m^{-3} above the freezing level, even in convection. The CLW content above the freezing level in convection during SMONEX in many cases was below 0.1 g m^{-3}. The CLW reduction was due to the large concentrations (approx. 800 L^{-1}) of ice particles at temperatures just below 0°C. Gamache (1990) found that most of the ice particles in stratiform regions came from the convective updrafts. Houze et al. (1992) studied the source regions for stratiform precipitation in Hurricane Norbert, which formed over the eastern Pacific in 1984. They concluded that most of the ice particles found in the stratiform regions came from convective cores.

Since CLW disappears within a few kilometers of the freezing level in convection and convective updrafts are the source regions for stratiform precipitation, it is reasonable to assume that little or no CLW exists in stratiform regions. Adler et al. (1991) found that the three-dimensional mesoscale model used in their study produced regions of stratiform precipitation where there was almost no CLW. At low rain rates, CLW is the most important factor influencing the upwelling radiation because the absorption from the relatively few precipitation-sized particles is not significant. The HCM assumes that low rain rates are produced by stratiform clouds, which have low CLW contents. Convective clouds have higher amounts of CLW but the effect of CLW is negligible at rain rates >5 mm h^{-1}, even at 37 GHz. Therefore, it is crucial that the CLW is correctly determined at rain rates <5 mm h^{-1}. Observations in stratiform regions effectively constrain the amount of CLW that clouds in the HCM can contain at low rain rates.

The CLW in the HCM is dependent on the rain rate. The WILM has a constant maximum CLW content of 0.5 g m^{-3} for rain rates <5 mm h^{-1}. Using results from observations, the CLW in the HCM is set at a maximum value of 0.1 g m^{-3} for rain rates <5 mm h^{-1}. The CLW in the HCM increases slowly as rain rate increases until around 10 mm h^{-1}, where a transition is made to convective rainfall. From this point, the CLW quickly rises to a maximum value of 1.2 g m^{-3} at 150 mm h^{-1}.

The vertically integrated value of CLW is important to upwelling brightness temperatures at low rain rates. In the WILM, the CLW was constrained to a 0.5-km layer below the freezing level producing an integrated CLW (ICLW) content of 0.03 g cm^{-2}. The HCM modifies the vertical CLW distribution to match observations made of CLW over the tropical oceans. The vertical CLW distribution is constructed so that it decreases linearly from a maximum CLW content at the cloud base to zero approximately 2 km above the freezing level. The height that the CLW reaches is dependent on the rain rate. Therefore, clouds with higher rain rates have a greater CLW depth. At low rain rates, the clouds in the HCM do not have any significant ICLW. At rain rates <5 mm h^{-1}, the ICLW is only 0.03 g cm^{-2}, which is identical to the WILM. It was shown earlier, that CLW does not extend very far above the freezing level, even in convection. The absence of large amounts of CLW above the freezing level in convection produces an ICLW content <0.5 g cm^{-2}. This number is significantly lower than the ICLW contents described in previous studies (e.g., Smith and Mugnai 1988) but a factor of 16 greater than in the WILM at high rain rates.

b. Changes to the vertical precipitation structure

Data from GATE showed researchers that the vertical reflectivity structure of tropical oceanic systems was

significantly different from midlatitude continental storms above the freezing level (Szoke et al. 1986; Zipser and Lutz 1994). Hurricanes and tropical storms also contained a similar vertical reflectivity structure as GATE cells (Black and Hallett 1986). A similar structure was observed in mesoscale systems during TAMEX (Jorgensen and LeMone 1989). Most studies have concluded that oceanic clouds contain a relatively constant reflectivity structure below the freezing level and a rapid decrease with height immediately above the freezing level to the top of the cloud. Continental systems share a similar structure below the freezing level but have a more gradual reflectivity decrease with height above the 0°C level.

GATE studies provided an explanation for the vertical reflectivity structure of oceanic clouds. The vertical profiles were caused by low updraft velocities promoting collision and coalescence, large raindrops >1 mm in diameter falling out before the freezing level was reached, and the absence of CLW below a temperature of -20°C (Szoke et el. 1986). The first factor would result in high rain rates from shallow convection. The second two of these three factors would cause the backscatter to drop off quickly above the freezing level since there were no large particles there. Also, the particles above the freezing level were mostly ice, which have an order of magnitude lower reflectivity than liquid drops of the same size (Jorgensen and LeMone 1989). The rain rates were weaker below the freezing level in stratiform clouds but similar to convection above the freezing level because convection had weak updrafts. The backscatter structure above the freezing level in stratiform clouds was due to falling and growing snow due to deposition, riming, and aggregation near the freezing level (Szoke et al. 1986).

Data from the warm pool showed that these clouds have a similar backscatter structure with height as GATE clouds (Williams et al. 1992; Zipser and Lutz 1994). Vertical reflectivity profiles of convective cells over Darwin, Australia, had maximum reflectivities below the freezing level and decreased rapidly above the freezing level (Zipser and Lutz 1994). Zipser and Lutz showed the lapse rate for the logarithm of the backscatter of ice was 6.5 dBZ km^{-1} in the TOGA COARE region with 6.0 dBZ km^{-1} in GATE—both a factor of 2–3 more than continental systems. It appears that most of the clouds observed during TOGA COARE have the identical vertical reflectivity structure as those described by Zipser and Lutz (1994).

The HCM modifies the precipitation structure above the freezing level. The model still assumes a constant rain rate below the freezing level as in the WILM. Observations showed that when CLW decreased above the freezing level so did the amount of liquid precipitation. The rapid conversion of liquid water into ice suggests that the total thickness of the supercooled water layer reaches no more than 1–2 km above the freezing level, even in strong convection. In response to this, the supercooled water layer in the HCM ranges from zero in stratiform clouds up to 1 km at 150 mm h^{-1}. Previous microphysical studies found that the rapid conversion of CLW and liquid water into ice above the freezing level was accompanied by a significant amount of small ice crystal production. The lack of any significant amount of large ice particles combined with the weak updrafts in oceanic clouds resulted in large gradients for the logarithm of the backscatter above the freezing level.

The HCM assumes a 6–8 dBZ km^{-1} lapse rate above the freezing level. A linear decrease in the logarithm of the backscatter of ice is the same as an inverse exponential decrease in the snowfall. Therefore, an exponential function is applied to the ice particles to maintain a linear lapse rate for the logarithm of the backscatter above the freezing level. The exponential ice decrease above the freezing level is considerably different than the assumptions made in the WILM. Since snowfall at a particular level in the model atmosphere is influenced by the number of precipitation-sized particles located there, a linear lapse rate for the logarithm of the backscatter of ice above the freezing level makes the ice layer much more transparent to microwave radiation by decreasing the amount and size of precipitation-sized particles.

c. Changes to the DSD

Measured DSDs vary widely, depending on the experiments created to measure them. The most commonly used DSD is the Marshall–Palmer (M–P) DSD (Marshall and Palmer 1948). DSDs can vary between stratiform and convective clouds due to the differences in the strength of the updraft. The radiative transfer model used in this paper uses an exponential fit for its DSD, although many studies use a gamma distribution. There has been a considerable amount of theoretical work done on DSDs (List and McFarquhar 1990; Brown 1988; Brown 1990). These studies suggested that DSDs were not exponential, such as the M–P DSD, but contained three peaks. The cause of the peaks was due to filament and sheet breakups (List and McFarquhar 1990). Filament breakups produced a peak in small drops, while sheet breakups caused a peak in medium-sized drops. Brown (1988; Brown 1990) found that the effects of filament, sheet, and disk breakup caused the DSD to reach an equilibrium state (i.e., the slope did not change as rain rate increased). The breakup of drops produced more small drops and fewer large drops than the M–P DSD. The M–P DSD was measured from continental clouds and was supposed to account for spontaneous drop breakup. However, spontaneous breakup was later found not to make a difference in the development of a DSD (List and McFarquhar 1990). The peaks produce a greater concentration of smaller drops than predicted by the M–P DSD (Valdez and Young 1985).

From observations taken during TOGA COARE, To-

kay and Short (1994) found from data taken on Kapingamarangi Atoll that from 1 to 10 mm h^{-1} convection had a large number of small to medium size drops <2 mm in diameter, while stratiform rain had more large drops. They pointed out that a M–P DSD did not fit the observed rainfall well. Jorgensen and Willis (1982) found that the *Z–R* relationship derived from the M–P DSD underestimated heavy rainfall in hurricanes. Willis and Tattelman (1989) also looked at tropical storms and hurricanes but with rain rates >25 mm h^{-1}. They found no drops >5 mm in diameter. The maximum drop sizes stabilized or even decreased at high rain rates. A smaller amount of large drops (>4 mm diameter) was found than predicted by the M–P DSD. They used a gamma distribution to fit the DSDs for high rain rates.

That TOGA COARE cells have small buoyancies (weak vertical velocities) means that there is more time for the warm rain process to act. Once the particles grow too large for the updraft to sustain, they fall out of the cloud. Jorgensen and LeMone (1989) and Black and Hallett (1986) both found that low updraft speeds in oceanic clouds observed in TAMEX and hurricanes, respectively, did not produce raindrops >3 mm in diameter in convection. Gamache (1990) looked at ice distributions above the freezing level in clouds during SMONEX. He found that concentrations of ice particles were greater in convective clouds than in stratiform clouds. Data suggested that the N_0 intercept for ice particles was greater than 10^8 m^{-4}. The DSD used in this paper will be an inverse-exponential DSD that contains a greater number of small precipitation particles and a fewer number of larger precipitation particles than the M–P DSD. As an example, the model uses a DSD intercept (N_0) of around 10^7 m^{-4} that is five times greater than the M–P DSD. A more detailed explanation of this DSD is left for a later discussion.

As will be discussed later, observations from TOGA COARE and other field projects have produced a new DSD. The DSD developed for this model is an inverse-exponential DSD similar to the M–P DSD. The distribution in terms of radius, φ, is

$$N(\varphi) = N_0 e^{-\Lambda\varphi}, \tag{1}$$

where

$$N_0 = 0.8 \text{ cm}^{-4},$$

$$\Lambda = \frac{120}{X^{0.23}} \text{ cm}^{-1}.$$

The variable X is a rain parameter used to vary the true rain rate. The true rain rate is computed by integrating the product of the drop volume and the Foote and duToit (1969) fall speed (ignoring up- or downdrafts) over the DSD. The rain parameter generated for this distribution is within 30% of the true rain rate for all rain rates calculated in the model. For comparison, the rain parameter for a M–P DSD is within 20% of the true rain rate.

The new DSD was developed from TOGA COARE observations (see section 7a) and data from other field projects. The DSD fits the observations of small ice particles above the freezing level and warm scattering signatures from MCSs during TOGA COARE. This DSD produces a greater number of small drops and fewer large drops than the M–P DSD. The combination of the new DSD and vertical precipitation structure above the freezing level results in an ice layer that is more transparent to microwave frequencies. The DSD can easily be converted to a *Z–R* relationship. The resulting equation is $Z = 103R^{1.61}$. Even though the new DSD is a significant departure from the M–P DSD, the changes in the derived rain rates are small for backscatter <35 dB*Z*.

Wilheit et al. (1977) showed that the *T–R* relationship at 19 GHz was relatively insensitive to the DSD in the increasing portion (low rain rate) of the *T–R* relationships. Also, the DSD does not significantly affect the *T–R* relationships at 18.7 and 21.3 GHz but the DSD has a larger effect at 13.8 and 37 GHz. The DSD used in the HCM is based on observations and seems to be more appropriate than the M–P DSD. The new DSD causes a lag in the response of the HCM at low rain rates and increases the dynamic range of each frequency at the high rain rate cutoff. Each frequency is sensitive to the DSD at different rain rates. For example, at 13.8 GHz the DSD affects the brightness temperatures around 10 mm h^{-1} since this part of the *T–R* relationship is highly sensitive to absorption from precipitation-sized particles. A M–P DSD causes the brightness temperatures to rise much more rapidly at low and moderate rain rates because it contains larger drops than the new DSD.

d. Changes to the angular distribution of reflected radiation from the ocean surface

Figure 1 shows convective and stratiform precipitation during TCM–90 in Supertyphoon Flo from 0932:43 to 0954 UTC 18 September 1990. The ocean surface is shown as a broad black horizontal line. False precipitation below the ocean surface was a result of double reflections from the ocean surface. For instance, the false bright band that appeared below the ocean surface in Fig. 1 was a result of the radiation from the radar that was reflected off the ocean surface, returned to the bright band, was reflected by rain drops there, returned to the ocean surface and finally, reflected back to the radar onboard the aircraft. The result is a mirror image that appears below the true ocean surface.

If the reflections from the ocean surface were diffuse, as in a Lambertian model, then there would be no clear pattern of false precipitation below the ocean surface. There is a possibility that a mirror image of the bright band would also appear if the ocean surface were rough, but the result would be a diffuse false bright band that is not the same distance from the ocean surface as the

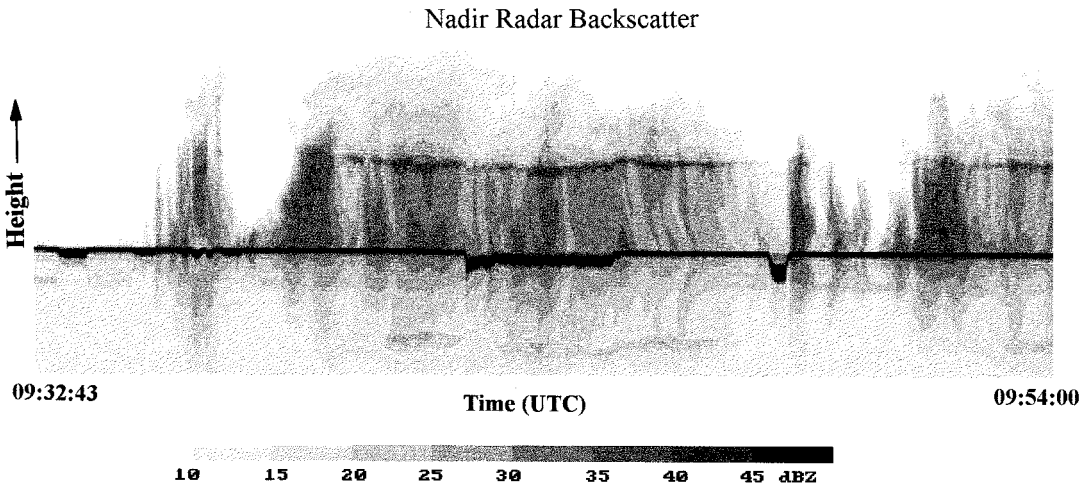

FIG. 1. Nadir backscatter observed by radar during TCM–90 in Super Typhoon Flo for 0932:43–0954 UTC 18 September 1990.

real bright band. A Lambertian ocean surface assumes that upwelling radiation leaving the ocean is a contribution from radiation approaching the ocean from many angles. The result is a maximum contribution from incoming radiation at approximately 45° from nadir. Since the majority of multiple reflections that would occur would be received at different angles, the false bright band would appear farther from the ocean surface and would be diffuse. Figure 1 shows that the false bright band was approximately the same distance from the ocean surface as the true bright band. The mirror images of the precipitation were distinct even outside of stratiform regions. Figure 1 serves to illustrate that the ocean surface appeared specular even within a typhoon. Radar data from TOGA COARE also indicated that a specular ocean surface assumption was more valid than the Lambertian assumption used by the WILM. The specular assumption assumes that the ocean surface acts like a mirror and only the incoming radiation that contributes to the upwelling brightness temperatures is from one incidence angle. This change in the ocean reflection results in brightness temperature differences of <5 K.

5. The HCM versus the WILM

The HCM is compared to the WILM using a 5-km freezing level at 4.5° incidence angle off nadir. The surface temperature for both models is set at 301 K with the WILM using a Lambertian ocean surface and the HCM using a specular surface. Figure 2 shows that the HCM produces colder brightness temperatures at low rain rates, the same brightness temperatures at saturation, and warmer brightness temperatures after saturation than the WILM at each frequency. At high rain rates, the HCM and the WILM appear to be similar based on brightness temperature alone, but both models assume different DSDs, precipitation structures, and surface reflectivities.

The ICLW content for both models are identical at low rain rates (0.03 g cm^{-2}) and IWVC is not significantly different (7.8 g cm^{-2} in the WILM vs 6.8 g cm^{-2} in the HCM). If the observations had shown that large amounts of CLW and high ice concentrations existed above the freezing level, then the HCM and the WILM would not be within 20 K at low rain rates. However, it has been shown that the precipitation and microphysics are not factors above the freezing level in tropical clouds over the dynamic range of each frequency at low rain rates. This is a result made by observations of small particles and vertical precipitation structure above the freezing level. Even though the HCM contains precipitation above the freezing level, the precipitation particles are small and few in number, and they contribute very little to the upwelling brightness temperatures. Therefore, the differences between the two models at 13.8 and 37 GHz at low rain rates are primarily a result of the DSD and angular distribution of reflected radiation from the ocean surface and, to a smaller degree, the IWVC. At viewing angles near nadir, a change from a specular to a Lambertian ocean surface amounts to differences of 5 K in the brightness temperatures generated by the HCM. At 18.7 and 21.3 GHz, the difference in IWVC between the HCM and WILM make water vapor more important at rain rates <3 mm h^{-1}. Differences in the IWVC of 1 g cm^{-2} are not significant at rain rates >3 mm h^{-1}, even at 18.7 and 21.3 GHz, because of the contribution from absorption by precipitation-sized particles. Therefore, TOGA COARE observations at low rain rates <3 mm h^{-1} are useful to determine whether the new DSD is correct at 37 GHz. The combination of larger drop sizes and Lambertian ocean surface in the WILM at low rain rates produces a net increase in brightness temperatures of 10–25 K above the HCM depending on the frequency.

It is interesting to note from Fig. 2 that 13.8 GHz has

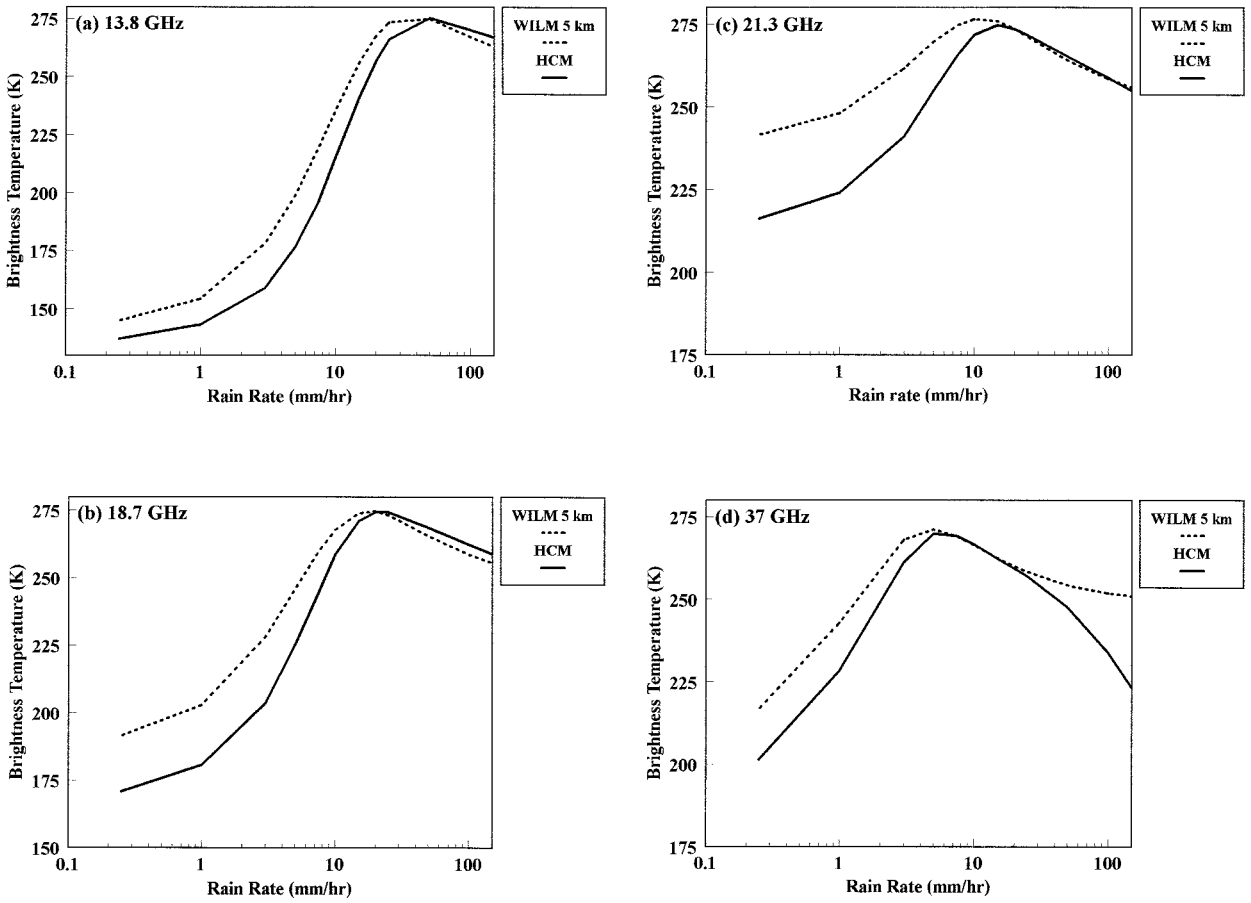

FIG. 2. *T–R* relationships generated by the HCM and the WILM at (a)13.8 GHz, (b) 18.7 GHz, (c) 21.3 GHz, and (d) 37 GHz.

approximately the same sensitivity to low rain rates as 18.7 GHz and, to a lesser extent, 21.3 GHz in the HCM. This is the result of the changes made to the CLW, vertical precipitation structure, and DSD at low rain rates. This conclusion is not identified in previous literature because most studies add a moderate amount of CLW at low rain rates, which results in a rapid change in the brightness temperatures as the frequency increases. However, in the HCM there is almost no CLW at low rain rates. This results in an increase in brightness temperatures based primarily on changes in the precipitation-sized particles. Observations will prove valuable to test this result.

At saturation, both models produce similar brightness temperatures at each frequency. However, this result is fortuitous because both models have substantially different thermodynamics and microphysics incorporated into them. The greater dynamic range and higher brightness temperatures generated by the HCM at moderate and high rain rates are a result of changes in the DSD since CLW does not influence the upwelling brightness temperatures at rain rates >5 mm h^{-1}. The reflectivity of the ocean surface is also not a factor at moderate and high rain rates since the opacity of the atmosphere dominates the changes made at the surface. Precipitation-sized particles above the freezing level have a noticeable effect at 37 GHz above 20 mm h^{-1}. However, the differences between the two models at these rain rates are of little practical significance since these rain rates lie well outside of the dynamic range at 37 GHz.

6. The HCM versus TOGA COARE observations

a. 2220–2225 UTC 10 February 1993

Figure 3 shows the vertical backscatter structure from ARMAR and the corresponding radiometer data for 2200–2225 UTC 10 February 1993 during TOGA COARE. The radar cross section clearly shows the surface (indicated by the broad black horizontal line) and the freezing level. Figure 3 shows that at least 4–5 km of ice was present above the freezing level in this system. The brightness temperatures from the radiometers were nearly constant for three-quarters of the time segment but began to rise at 2224 UTC. The time segment of interest (2220–2224 UTC) was an area where the radar was barely detecting rainfall at the surface. For most of this region, the radar indicated a backscatter

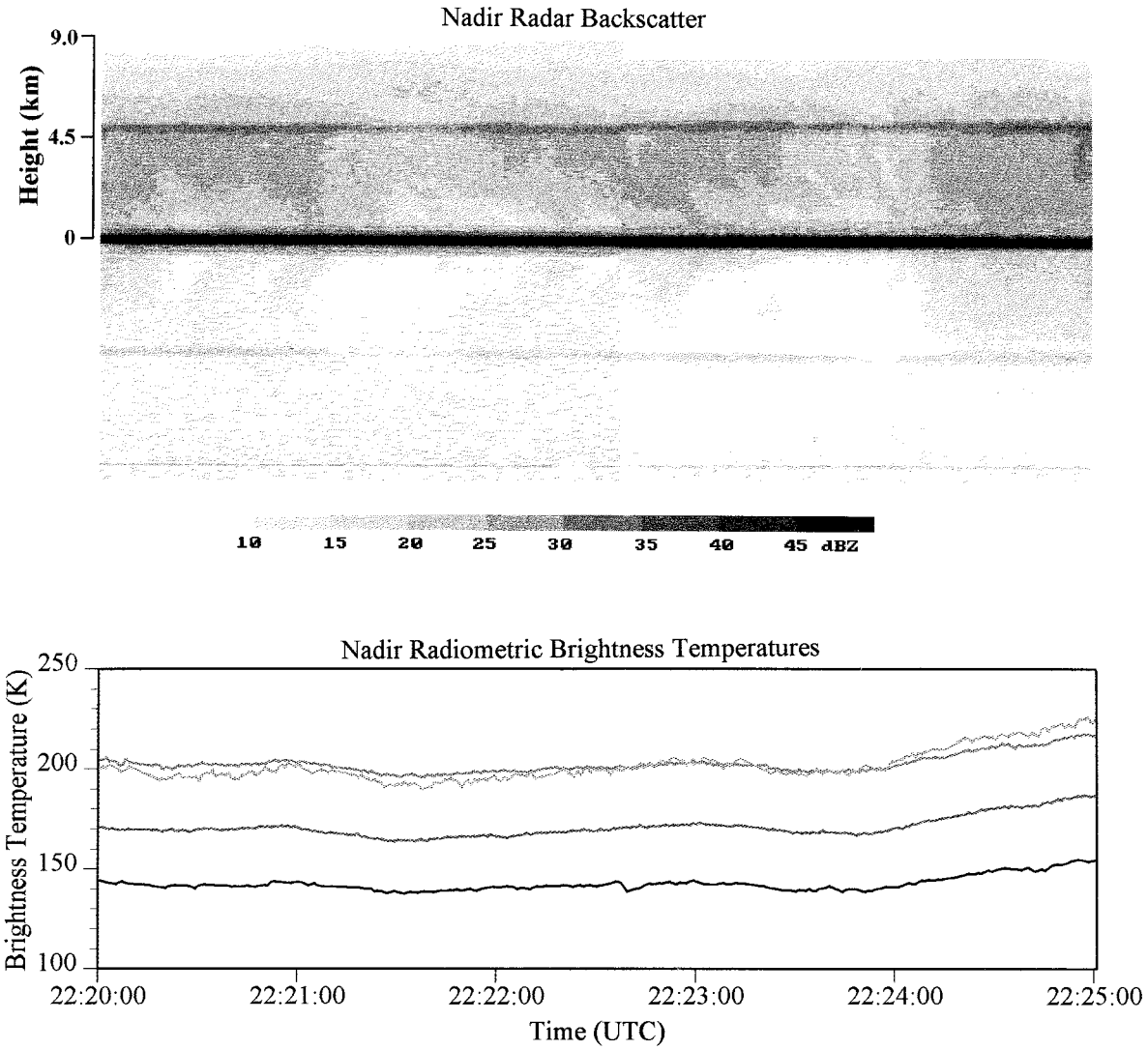

FIG. 3. Nadir backscatter observed by ARMAR and corresponding nadir radiometric brightness temperatures observed by ARMAR and AMMR at 13.8, 18.7, 21.3, and 37 GHz for 2200–2225 UTC 10 February 1993 during TOGA COARE. The radiometer traces from black to light gray correspond to 13.8, 18.7, 21.3, and 37 GHz, respectively.

between 10 and 20 dBZ, which equated to rain rates <1 mm h^{-1}. In several sections, the backscatter had fallen below the minimum detectable rain rate near the ocean surface (<0.2 mm h^{-1}). The uniformity of the observed brightness temperatures at 37 GHz indicated that there was not much variation in the rainfall or CLW content.

The HCM predicts values of 137, 170, 216, and 201 K at 13.8, 18.7, 21.3, and 37-GHz, respectively, for a path average rain rate of 0.25 mm h^{-1} (Fig. 2). The observations show that 37-GHz brightness temperatures averaged 200 K from 2220 to 2224 UTC. The similarity between the brightness temperatures generated by the HCM and observations indicates that the model handles CLW correctly at low rain rates. The water vapor profile is not a factor at 37 GHz. The observations show an average of 140, 170, and 208 K at 13.8, 18.7, and 21.3 GHz, respectively, from 2220 to 2224 UTC. The HCM agrees closely with the observed brightness temperatures at each frequency for a rain rate of approximately 0.25 mm h^{-1}. The estimated path-average rain rate between the surface and freezing level from the HCM agrees well with the radar.

The HCM and WILM have the same ICLW content (0.03 g cm^{-2}) at low rain rates. The microphysics in the HCM at low rain rates makes it identical to the WILM above the freezing level. The combination of the new DSD, vertical precipitation structure, and lower IWVC in the HCM makes the cloud more transparent to microwave frequencies <37 GHz. From the previous section, the differences between the HCM and the WILM at low rain rates <3 mm h^{-1} are primarily a result of changes in the angular distribution of reflected radiation

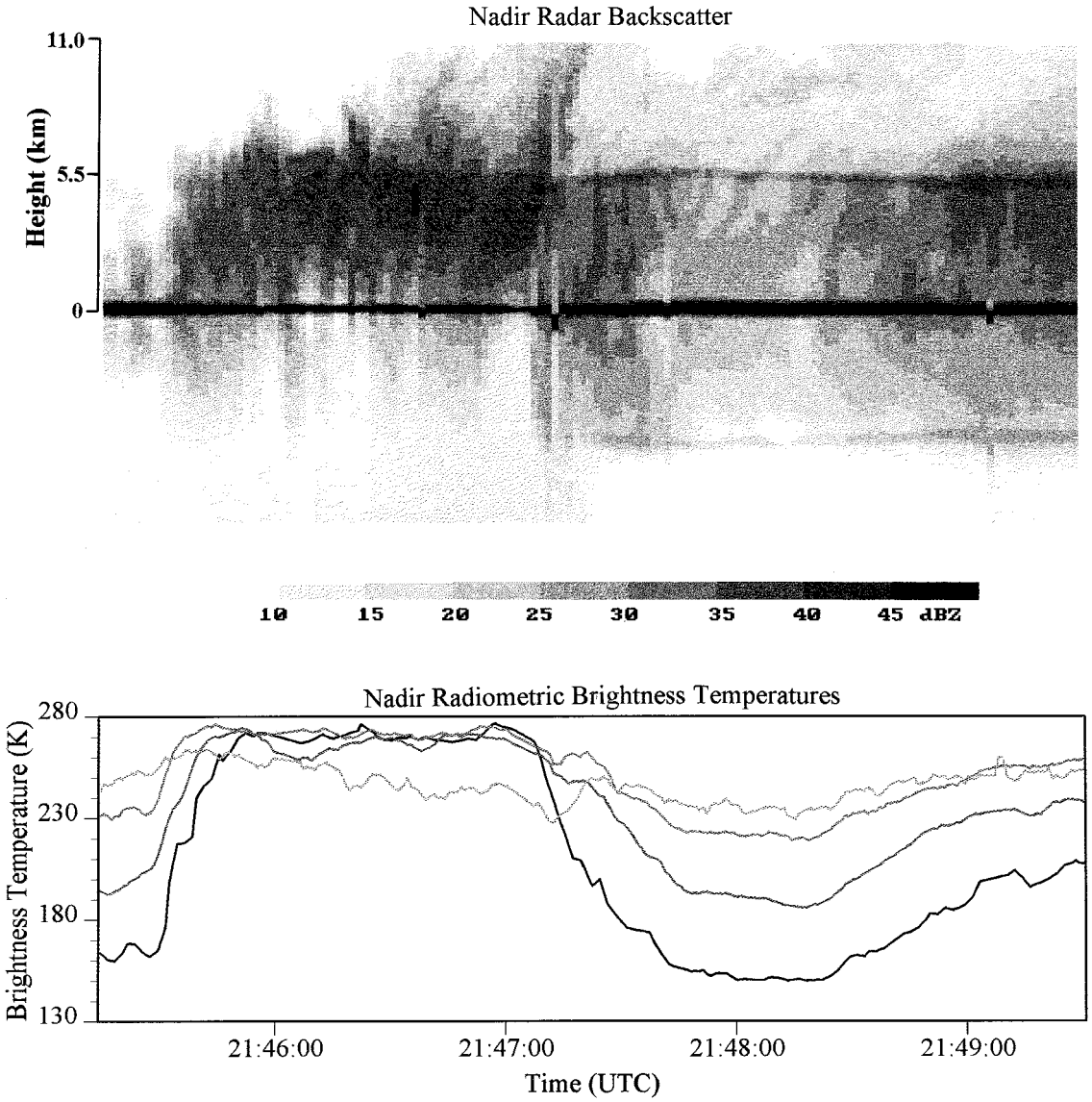

FIG. 4. As in Fig. 3, except from 2145:14 to 2149:30 UTC 20 February 1993.

from the ocean surface and the DSD at 13.8 and 37 GHz. The differences become larger at 18.7 and 21.3 GHz due to the difference in the IWVC between the HCM and the WILM. Since the differences in the upwelling brightness temperatures are a result of changes in the angular distribution of reflected radiation from the ocean surface are approximately 5 K, any large differences between the HCM and the WILM at 37 GHz are a result of the differences between the M–P DSD and the new DSD since small differences in IWVC at this frequency are negligible. At 37 GHz, the HCM and the WILM differ by 15 K at rain rates <1 mm h^{-1} (Fig. 2d). The brightness temperatures generated by the WILM are the result of the increased opacity in the model atmosphere created by the absorption of large drops produced by the M–P DSD. The WILM overestimates the observed brightness temperatures by at least 10 K in this region if the ocean reflectivity is taken into account. The new DSD brings the HCM closer to the observations.

b. 2145:14–2149:30 UTC 20 February 1993

Figure 4 shows radar and radiometer measurements of a convective line-trailing stratiform region observed from 2145:14 to 2149:30 UTC 20 February 1993 during TOGA COARE. The radar became partially attenuated as it passed over the convection. The attenuation was indicated by lower backscatter near the surface from 2146 to 2147 UTC. As a result, an average backscatter of 45 dB*Z* (35 mm h^{-1}) in this region was an underestimate. The convection appeared to be confined to

below the freezing level around 2146 UTC, indicating that the warm rain process was probably prevalent there. However, by 2146:30 UTC ice appeared above the freezing level, indicating that a cold rain process had developed. The system became more stratiform at 2147:30 UTC. The stratiform region contained areas of very light to moderate rainfall with an extensive layer of ice above the freezing level.

The observed brightness temperatures at 13.8, 18.7, and 21 GHz were approximately 270 K in the convective line, while the 37 GHz varied between 230 and 260 K. Curiously, brightness temperatures in excess of 270 K at 13.8 GHz indicated a surface rain rate >30 mm h^{-1} but 18.7 and 21.3 GHz remained well above 260 K. The high brightness temperatures at high rain rates at 18.7 and 21.3 GHz indicated the absence of large ice particles above the freezing level. This, combined with observations by Gamache (1990), led to the introduction of a new DSD containing fewer large precipitation particles and a higher number of small precipitation particles.

The 37-GHz channel brightness temperatures showed a minimum of 230 K at 2147:15 UTC as a significant number of ice particles appeared above the freezing level. After 2147:30 UTC, the rainfall decreased and became more stratiform. At 2148 UTC, the backscatter of 24 dB*Z* (1.7 mm h^{-1}) was slightly higher than at 2224–2225 UTC 10 February (Fig. 3). As a result, the observed brightness temperatures at 2148 UTC 20 February were nearly the same and slightly higher than 2224–2225 UTC 10 February. As the rainfall increased in the stratiform region at 2149 UTC, the brightness temperatures increased 10–50 K. Radar indicated a surface rain rate of around 8 mm h^{-1} (34 dB*Z*) in this region.

The warm brightness temperatures of 275 K in the convective region from 2145:14 to 2149:30 UTC are easily reproduced by the HCM. The region of observed brightness temperatures >270 K at 13.8 GHz is indicated by the HCM as having a path-average rain rate between the surface and freezing level of >35 mm h^{-1}. Radar indicated a similar rain rate with a slightly attenuated backscatter around 45 dB*Z* (35 mm h^{-1}). The HCM indicates that 18.7 and 21.3 GHz should remain near 270 K, even at 35 mm h^{-1}. This is verified by the observations. The 37-GHz channel became saturated as it passed over the convective line. The HCM predicts a brightness temperature of around 250 K for a 35 mm h^{-1} rain rate. The brightness temperature predicted by the HCM is close to the majority of observed 37-GHz brightness temperatures in this region. The 37-GHz channel is not important for path-averaged rain rate measurements in the convective line; however, it does indicate whether the HCM handles the precipitation structure above the freezing level correctly.

The observations provided important information about the effect of ice on the upwelling brightness temperatures. In the HCM, the ice layer contains a high concentration of small ice particles that decreases rapidly with height, which makes the ice layer transparent at frequencies <37 GHz, even if it has a thickness of 6 km. An inspection of the observed 37-GHz brightness temperatures throughout Fig. 4 shows that this frequency only varied by 20 K over the entire time segment. This small variation is remarkable considering that the observations indicated heavy precipitation with no precipitation above the freezing level, heavy rain with a significant amount of ice above the freezing level (at 2147:15 UTC), and stratiform rain. The HCM predicts a range of 20 K at 37 GHz for rain rates of 5–50 mm h^{-1}. At 13.8, 21.3, and 18.7 GHz the effect of ice is even less noticeable. For instance, within the convective line the observed brightness temperatures remained constant even though the precipitation structure above the freezing level went from no ice to 6 km of ice.

A stratiform precipitation region was seen after 2147:30 UTC. This area was characterized by light to moderate rain. At 2148 UTC the radar indicated a rain rate of approximately 1.7 mm h^{-1} (24 dB*Z*). The HCM closely agrees with the radiometer brightness temperatures for the same rain rate. Radar observations indicated that rainfall increased at 2149 UTC to around 8 mm h^{-1} (34 dB*Z*). Again, the brightness temperatures generated by the HCM agree with the observations and are all within a factor of 2 of the radar-estimated rain rate. A comparison between observed 13.8-, 18.7-, and 21.3-GHz brightness temperatures in this area showed that the 13.8 GHz had the same sensitivity to low rain rates as the two higher frequencies. This result was predicted by the HCM.

c. 2131:30–2136 UTC 22 February 1993

Figure 5 shows an MCS observed from 2131:30 to 2136 UTC 22 February 1993. The radar data revealed a classic MCS containing a leading convective line (2135 UTC) and a trailing stratiform region (2132–2134:30 UTC). The radar became attenuated at 2135 UTC because of a large amount of precipitation-sized particles (probably containing graupel) located near the freezing level. The convective line tilted from east to west (west is located on the left-hand side of the image). Shear carried precipitation through the convective line and into the stratiform region to the west.

The HCM assumption that the majority of low rain-rate observations comes from stratiform clouds is examined in this MCS. In Fig. 5, the number of low rain rate stratiform observations exceeded the number of observations in growing convective cells with the same rain rate by a ratio of $>100:1$. The only region that contained growing convective cells with light precipitation could only have occurred around 2135 UTC, while stratiform precipitation was prevalent from 2132 to 2134 UTC.

Since 37 GHz was saturated for most of the system, any quantitative measurement of the rain rate was lost. However, it is worth mentioning that 37 GHz decreased

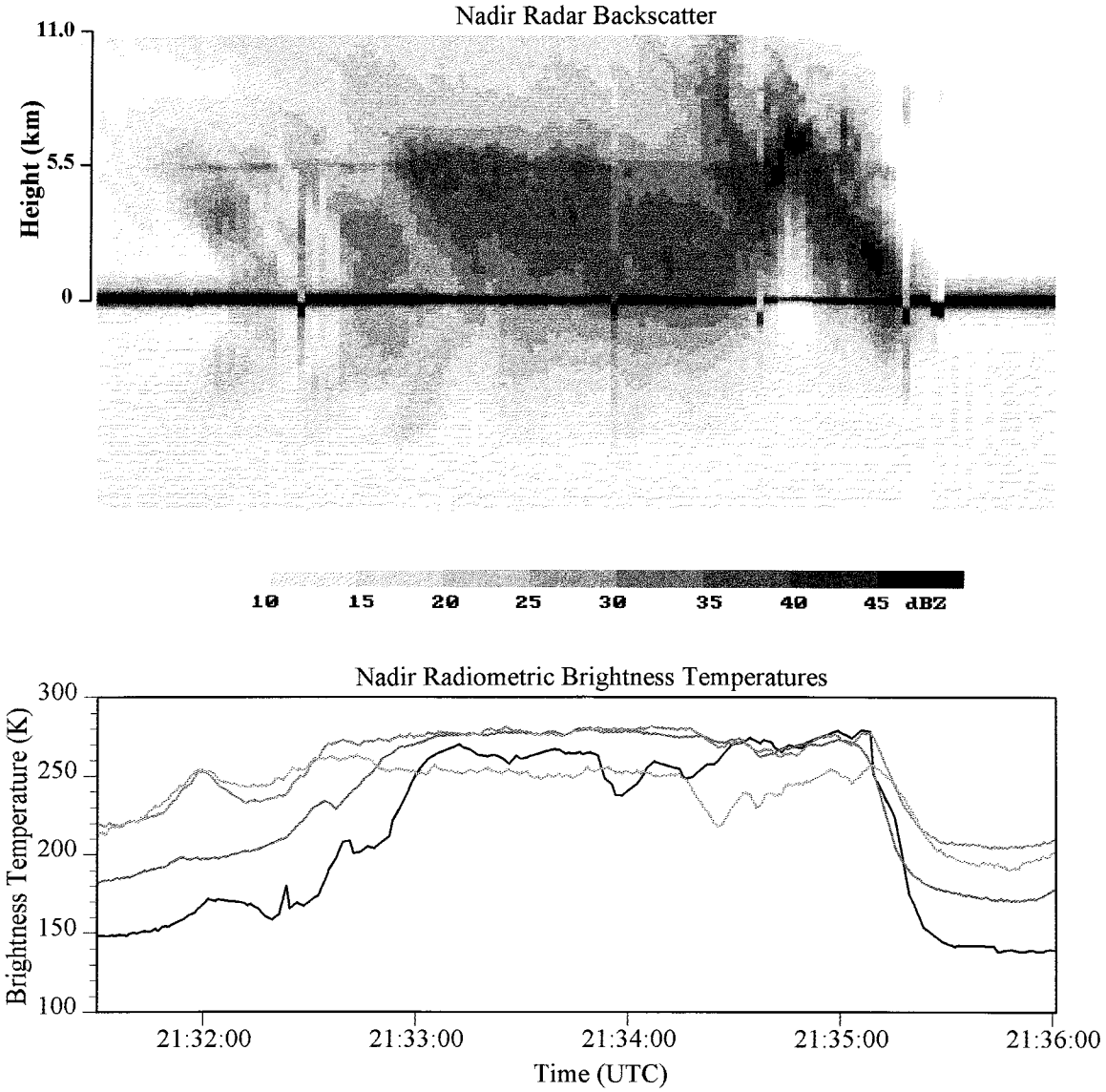

FIG. 5. As in Fig. 3, except from 2131:30 to 2136 UTC 22 February 1993.

to a minimum of 220 K between 2134 and 2135 UTC when a considerable amount of precipitation appeared above the freezing level. The brightness temperatures at 13.8, 18.7, and 21.3 GHz indicated that the rain rate was lower than in the convective line farther east. The high shear in the system displaced the greatest amount of precipitation above the freezing level away from the heaviest surface rainfall. Microwave algorithms that base their rain rate retrievals on the scattering of precipitation-sized particles above the freezing level would misinterpret the surface rain rate in this system.

The stratiform region observed between 2132 and 2134:30 UTC was unusual because it produced rain rates that were normally considered convective. Radar indicated an average near-surface backscatter of 38 dBZ (13 mm h^{-1}). However, Fig. 5 shows an obvious bright band in this region. The 18.7-GHz and 21.3-GHz frequencies were saturated in this region, making them insensitive to changes in the rain rate below the freezing level. The HCM interprets the brightness temperatures at 18.7 and 21.3 GHz as having a rain rate between 15 and 20 mm h^{-1}. Between 2133 and 2134:30 UTC, the 13.8-GHz brightness temperatures ranged from 230 to 260 K, which is interpreted by the HCM as a rain rate of 12–23 mm h^{-1}. The brightness temperatures at 13.8 GHz were stable enough between 2133 and 2133:50 UTC to test the DSD used by the HCM. Unfortunately, the rain rate in this region reduced the sensitivity to the DSD at 13.8 GHz to near the accuracy of the radiometers. The HCM using a M–P DSD still estimates a rain rate slightly lower than the HCM using a new DSD but is still within a factor of 2 of the radar.

Radar attenuation in the convective region (around 2135 UTC) made it impossible to estimate surface rain rate. However, it was possible to estimate a path-average rain rate from the radiometers. The 13.8-GHz brightness temperatures rose to >270 K, while brightness temperatures at 18.7 and 21.3 GHz decreased, probably due to scattering from large precipitation-sized particles near the freezing level. Assuming 13.8 GHz was not saturated, the HCM suggests a rain rate >40 mm h^{-1} in this region. At this rain rate, 18.7 and 21.3 GHz would remain above 265 K in the HCM (Fig. 2). The observations show that these two frequencies do not fall below 260 K. Assuming the HCM handles the precipitation structure above the freezing level correctly, lower brightness temperatures at 18.7 and 21.3 GHz in the convective line were not a result of scattering by ice above the freezing level but a result of the scattering by large rain drops below the freezing level.

7. Conclusions

An improved microwave radiative transfer model was developed to simulate observed brightness temperatures from tropical oceanic clouds with rain. The HCM uses a one-dimensional cloud model integrated along the vertical axis. The simplicity of the cloud model in the HCM allowed the alteration of relevant thermodynamic and microphysical profiles according to observations. It was shown that a plane-parallel radiative transfer model based on fundamental physics coupled with a one-dimensional cloud model can produce brightness temperatures that correspond closely to the observations if the microphysics and angular distribution of reflected radiation from the ocean surface are accurately described.

Observations from previous field studies had shown that CLW and vertical backscatter decreased rapidly above the freezing level for all rain rates The amount of CLW was found to be near zero in stratiform areas from modeling and observational studies. The rapid conversion of liquid water into ice and the production of numerous small ice crystals led to steep backscatter lapse rates above the freezing level. Studies found that a linear lapse rate for the logarithm of the backscatter of ice was common for tropical oceanic convection. A linear decrease in the logarithm of the backscatter of ice is the same as an inverse exponential decrease in the snowfall above the freezing level. Observational and theoretical work has shown that the M-P DSD does not describe the DSD in tropical clouds. The M–P DSD continually overestimates the number of large drops and underestimates the number of small drops. A new DSD was created to increase the number of small drops and decrease the number of large drops.

Radar data from TCM–90 and TOGA COARE show that the ocean surface is specular. If a specular surface is assumed, the resulting brightness temperatures would be approximately 5 K lower at low and moderate rain rates, even at incidence angles near nadir. A Lambertian ocean used by the WILM assumes that the upwelling brightness temperatures are a result of a contribution from downwelling radiation from many angles. A specular ocean acts like a flat mirror so only downwelling radiation at one angle contributes to the upwelling radiation; therefore, for near-nadir observations, the upwelling brightness temperatures are lower than those generated by a Lambertian ocean surface. The HCM was created to incorporate the changes to the CLW, vertical precipitation structure, DSD, and angular distribution of reflected radiation from the ocean surface.

The HCM assumes that low rain rates are produced by stratiform clouds. If the HCM assumes that the microphysics present in the cloud at low rain rates is associated with stratiform clouds and that high rain rates originate by convective clouds, then the model represents a cloud evolution over the dynamic range of each frequency.

The comparison between the HCM and the WILM showed that there were as much as 25 K differences between the two models at low rain rates at 18.7 and 21.3 GHz. The differences were primarily a result of changes in the DSD and IWVC and to a lesser extent, the angular distribution of reflected radiation from the ocean surface at 18.7 and 21.3 GHz. The change in angular distribution of reflected radiation from the ocean surface at nadir produces an approximately 5-K change in brightness temperatures at all frequencies. Although the differences in water vapor profiles between the HCM and the WILM cannot be ruled out at 18.7 and 21.3 GHz (approximately 15 K), the 37-GHz channel was used to test the DSD at low rain rates since it is not sensitive to water vapor. At moderate and high rain rates, the two models are nearly identical but for different reasons. The DSD and vertical precipitation structure in the HCM produces the same result as the absence of precipitation above the freezing level and the M–P DSD in the WILM.

Next, the HCM was compared to observations from TOGA COARE. The similarity between the HCM and the observations for all rain rates showed that the microphysics above the freezing level had no effect at 13.8, 18.7, and 21.3 GHz. The microphysics affected 37 GHz at high rain rates but well beyond the dynamic range of the frequency. The brightness temperatures generated by the HCM at 37 GHz were close to the observations at low rain rates. This indicates that the model handles the CLW correctly in stratiform regions. The warm brightness temperatures observed in convection at moderate and high rain rates was also accurately simulated by the HCM. The warm upwelling brightness temperatures generated by the HCM at 13.8, 18.7, 21.3, and 37 GHz were a result of the changes to the DSD and vertical precipitation structure above the freezing level. The new DSD in the HCM was verified by the observations at low rain rates. The brightness temperature differences of approximately 15 K between the HCM and the WILM at low rain rates were mainly a result

of the changes in the DSD. Since the HCM was similar to the observations, the new DSD appears to be a better approximation than the M–P DSD.

The HCM consistently produced rain rates that were within a factor of 2 of the radar-estimated rain rate. However, backscatter from radar is unreliable because it relies on the sixth moment of the drop radius as well as having calibration difficulties. This uncertainty is carried over to the *Z–R* relationship, which estimates a surface rainfall from radar backscatter. Therefore, radar cannot be considered a reliable method for determining the rain rate ''ground truth.'' The primary reason that the radar and radiometer data correspond closely with each other was due to the way the *Z–R* relationship was determined. Observational and theoretical work combined to produce a *Z–R* relationship that originated from a new DSD. New methods for determining rainfall, such as the development of a new DSD from microwave and microphysical observations, may be necessary to produce ground truth for TRMM.

Acknowledgments. Special thanks goes to the Jet Propulsion Laboratory for providing the ARMAR vertical backscatter and radiometer data. The authors would also like to thank the Goddard Space Flight Center for providing the AMMR data. This research was supported by NASA Grants NAG-5-1423 and NAG-5-1568.

REFERENCES

Adler, R. R., H. Y. M. Yeh, N. Prasad, W. K. Tao, and J. Simpson, 1991: Microwave simulations of a tropical rainfall system with a three-dimensional cloud model. *J. Appl. Meteor.,* **30,** 924–953.

Bauer, P., and P. Schluessel, 1993: Rainfall, total water, ice water, and water vapor over sea from polarized microwave simulations and Special Sensor Microwave/Imager data. *J. Geophys. Res.,* **98,** 737–759.

Black, R. A., and J. Hallett, 1986: Observations of the distribution of ice in hurricanes. *J. Atmos. Sci.,* **43,** 802–822.

Brown, P. S., Jr., 1988: The effects of filament, sheet, and disk breakup upon the drop spectrum. *J. Atmos. Sci.,* **45,** 712–718.

——, 1990: Reversals in evolving raindrop size distributions due to the effects of coalescence and breakup. *J. Atmos. Sci.,* **47,** 746–754.

Chang, A. T. C., and T. T. Wilheit, 1979: Remote sensing of atmospheric water vapor, liquid water and wind speed at the ocean surface by passive microwave techniques from the *Nimbus*-5 satellite. *Radio Sci.,* **14,** 793–802.

Foote, C. B., and P. S. duToit, 1969: Terminal velocity of raindrops aloft. *J. Appl. Meteor.,* **8,** 249–253.

Gamache, J. F., 1990: Microphysical observations in summer MONEX convective and stratiform clouds. *Mon. Wea. Rev.,* **118,** 1238–1249.

Houze, R. A., Jr., F. D. Marks, and R. A. Black, 1992: Dual-aircraft investigation of the inner core of Hurricane Norbert. Part II: Mesoscale distribution of ice particles. *J. Atmos. Sci.,* **49,** 943–962.

Jorgensen, D. P., and P. T. Willis, 1982: A *Z–R* relationship for hurricanes. *J. Appl. Meteor.,* **21,** 356–366.

——, and M. A. LeMone, 1989: Vertical velocity characteristics of oceanic convection. *J. Atmos. Sci.,* **46,** 621–640.

Kummerow, C., and L. Giglio, 1994a: A passive microwave technique for estimating rainfall and vertical structure information from space. Part I: Algorithm description. *J. Appl. Meteor.,* **33,** 3–18.

——, and ——, 1994b: A passive microwave technique for estimating rainfall and vertical structure information from space. Part II: Applications to SSM/I data. *J. Appl. Meteor.,* **33,** 19–34.

List, R., and G. M. McFarquhar, 1990: The role of breakup and coalescence in the three-peak equilibrium distribution of raindrops. *J. Atmos. Sci.,* **47,** 2274–2292.

Lucas, C., E. J. Zipser, and M. A. LeMone, 1994: Vertical velocity in oceanic convection off tropical Australia. *J. Atmos. Sci.,* **51,** 3183–3193.

Marshall, T. S., and W. Mck. Palmer, 1948: The distribution of raindrops with size. *J. Meteor.,* **5,** 165–166.

Mugnai, A., and E. A. Smith, 1988: Radiative transfer to space through a precipitating cloud at multiple microwave frequencies. Part I: Model description. *J. Appl. Meteor.,* **27,** 1055–1073.

——, ——, and G. J. Tripoli, 1993: Foundations for statistical–physical precipitation retrieval from passive microwave satellite measurements. Part II: Emission-source and generalized weighting-function properties of a time-dependent cloud-radiation model. *J. Appl. Meteor.,* **32,** 17–39.

Simpson, J. R., R. F. Adler, and G. R. North, 1988: A proposed tropical rainfall measuring mission (TRMM) satellite. *Bull. Amer. Meteor. Soc.,* **69,** 278–295.

Smith, E. A., and A. Mugnai, 1988: Radiative transfer to space through a precipitating cloud at multiple microwave frequencies. Part II: Results and analysis. *J. Appl. Meteor.,* **27,** 1074–1091.

——, ——, H. J. Cooper, G. J. Tripoli, and X. Xiang, 1992: Foundations for statistical–physical precipitation retrieval from passive microwave satellite measurements. Part I: Brightness-temperature properties of a time-dependent cloud-radiation model. *J. Appl. Meteor.,* **31,** 506–531.

Szoke, E. J., E. J. Zipser, and D. P. Jorgensen, 1986: A radar study of convective cells in mesoscale systems in GATE. Part I: Vertical profile statistics and comparison with hurricanes. *J. Atmos. Sci.,* **43,** 182–197.

Tokay, A., and D. A. Short, 1994: Case studies of convective vs stratiform rain over Kapingamarangi atoll during TOGA-COARE. Preprints, *Sixth Conf. on Mesoscale Processes,* Portland, OR, Amer. Meteor. Soc., 85–88.

Valdez, M. P., and K. C. Young, 1985: Number fluxes in equilibrium raindrop populations: A Markov chain analysis. *J. Atmos. Sci.,* **42,** 1024–1036.

Wang, S. A., 1997: Modeling the beamfilling correction for microwave retrieval of oceanic rainfall. Ph.D. thesis, Texas A&M University, 100 pp.

Wilheit, T. T., A. T. C. Chang, M. S. V. Rao, E. B. Rodgers, and J. S. Theon, 1977: A satellite technique for quantitatively mapping rainfall rates over the ocean. *J. Appl. Meteor.,* **16,** 551–560.

Williams, E. R., S. A. Rutledge, S. G. Geotis, N. Renno, E. Rasmussen, and T. Rickenbach, 1992: Radar and electrical study of tropical ''hot towers.'' *J. Atmos. Sci.,* **49,** 1386–1395.

Willis, P. T., and P. Tattelman, 1989: Drop-size distributions associated with intense rainfall. *J. Appl. Meteor.,* **28,** 3–15.

Zipser, E. J., and M. A. LeMone, 1980: Cumulonimbus vertical velocity events in GATE. Part II: Synthesis and model core structure. *J. Atmos. Sci.,* **37,** 2458–2469.

——, and K. R. Lutz, 1994: The vertical profile of radar reflectivity of convective cells: A strong indicator of storm intensity and lightning probability? *Mon. Wea. Rev.,* **122,** 1751–1759.